

Surface lattice dynamics of rutile TiO₂(110) using helium atom surface scatteringE. A. Akhadow,¹ S. A. Safron,² J. G. Skofronick,¹ D. H. Van Winkle,¹ F. A. Flaherty,³ and Rifat Fatema¹
¹MARTECH and Department of Physics, Florida State University, Tallahassee, Florida 32306, USA²MARTECH and Department of Chemistry and Biochemistry, Florida State University, Tallahassee, Florida 32306, USA³Physics Department, Valdosta State University, Valdosta, Georgia 31698, USA

(Received 7 October 2002; revised manuscript received 21 January 2003; published 3 July 2003)

The lattice dynamics of the rutile TiO₂(110) surface has been investigated by means of high-resolution helium atom scattering (HAS) techniques over the temperature range of ~ 100 – 1000 K. HAS diffraction in the $\bar{\Gamma}X$, $\bar{\Gamma}S$, and $\bar{\Gamma}Y$ surface Brillouin zone directions indicates that almost the entire surface retains the bulk termination (1×1) structure under the preparation conditions employed. Surface phonon dispersion curves in the $\bar{\Gamma}X$, $\bar{\Gamma}S$, and $\bar{\Gamma}Y$ regions of the surface Brillouin zone, obtained through inelastic atom scattering measurements of single-phonon creation and annihilation events, reveal changes in the surface forces as the temperature of the surface varies. Although model calculations for the dynamics of this surface are not currently available, the observed modes are interpreted, in part, by comparison with calculations reported for the rutile MgF₂(110) surface.

DOI: 10.1103/PhysRevB.68.035409

PACS number(s): 68.35.Ja, 68.49.Bc, 68.47.Gh, 68.35.Bs

I. INTRODUCTION

Helium atom scattering (HAS) is remarkably useful for acquiring data which, combined with model calculations, provide information on the structure and surface dynamics of crystalline surfaces of all types.^{1–11} In particular, the work carried out on ionic insulators has been of special importance since for these materials other surface probes (predominantly electrons and ions) have often had problems with surface charging and damage.¹² Early HAS dynamics studies on insulator surfaces began with the alkali halides^{9–11} and were followed by experiments on rocksalt-structured metal oxide crystals such as MgO, CoO, and NiO. Despite their different chemistries, these similarly structured crystalline materials were found to exhibit similar dynamical behaviors.^{13–19} The effective combination of experiments with theory has led in more recent work to considerable advances in understanding the behaviors of more complex materials such as the ABO₃ perovskites.^{20–25}

Bulk rutile TiO₂ has been investigated experimentally by Traylor *et al.* using neutron scattering²⁶ and theoretical modeling has been carried out for the bulk lattice dynamics of a number of crystals with the rutile structure.^{27–29} However, neither experimental work nor theoretical modeling has been reported for the surface dynamics of rutile TiO₂. Nevertheless, the interpretation of the data reported in this paper is guided in part by comparison with the shell model calculations for the surface phonon dispersion in the three high-symmetry directions of the rutile MgF₂ (110) surface Brillouin zone (SBZ).³⁰

Extensive structural studies of TiO₂ (110), employing scanning tunneling microscopy (STM) and low-energy ion scattering under ultrahigh-vacuum conditions, have been carried out by the group of U. Diebold on clean surfaces as well as on the effects of oxygen and sulfur adsorbates dosed onto these surfaces after treatment at high temperatures.^{31,32} Their reported STM images, although taken at room temperature, serve as important benchmarks for the temperature-dependent helium diffraction results reported here.

The early HAS investigations of the dynamics of the alkali halides and other rocksalt crystals dealt with materials having bulk unit cells composed of only two ions, and as HAS research matured, more complex materials with three or more ions in the unit cell have been examined.^{33–36} In the work reported here for rutile TiO₂, the bulk unit cell contains six ions from two TiO₂ units. Clearly, the increased number and complexity of the lattice vibrations for these rutile-structured materials present considerable challenges to both experimenters and theorists. However, for the same reasons the surfaces of these materials are more interesting and technologically significant than those of the simpler rocksalt materials which have been rather thoroughly studied.^{13–18,37}

In the following section, we first give brief descriptions of the HAS instrument, the target preparation, and the helium scattering experiments that were carried out. The next section is devoted to a brief presentation of helium diffraction measurements establishing the surface structure. After that we focus on the time-of-flight (TOF) measurements (the main topic of this research) and the surface phonon dispersion curves obtained from them; in addition, we discuss the character of the observed vibrational modes. In the final section the conclusions from these experiments are summarized.

II. EXPERIMENT

The probing of crystalline surfaces with neutral, thermal energy helium atoms is now a well-established technique and has been described in detail in several articles.^{11,38–40} Figure 1 shows a schematic of the FSU instrument which has been designed primarily for inelastic scattering experiments. It consists of three main sections: (i) beam source, (ii) scattering chamber, and (iii) TOF/detector. A nearly monoenergetic ($\Delta v/v \approx 0.8\%$), high-intensity, neutral helium atom beam is produced by expanding helium gas at ~ 25 – 30 bar pressure through a nominally 30 - μm -diam nozzle. The wave vector (or kinetic energy) of the atoms in the beam is controlled by the nozzle temperature which is adjusted by changing the balance between a closed-cycle mechanical refrigerator and a

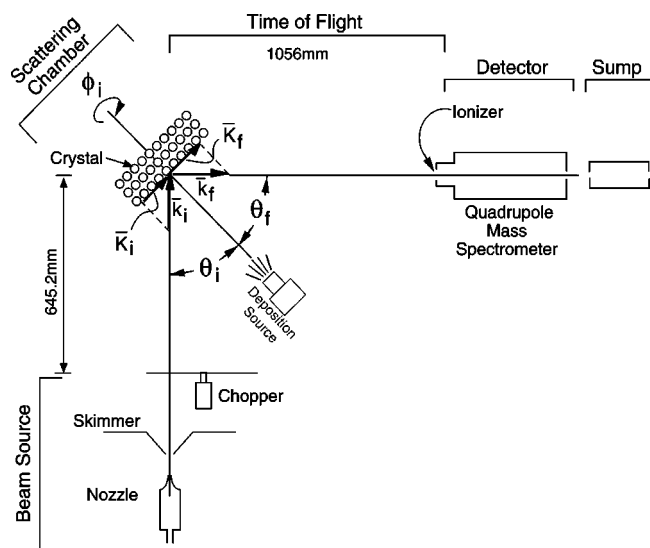


FIG. 1. Schematic of the helium atom scattering (HAS) instrument. The 90° geometry of the source-to-target and target-to-detector axes and the incident and final angles and wave vectors of the beam are indicated.

heater operated in feedback mode. This arrangement produces nozzle temperatures from 70 K to 325 K, corresponding to incident helium wave vectors (energies) from about 5.5 \AA^{-1} (16 meV) to 11.7 \AA^{-1} (67 meV). The retractable chopper provides 800 Hz helium atom pulses with $22\text{-}\mu\text{s}$ full-width-half-maximum (FWHM) time widths. For angular distribution measurements of the helium diffraction the chopper is translated out of the beam line.

The scattering chamber is separated from the beam source by three stages of differential pumping and its background pressure typically lies in the low 10^{-10} mbar regime. The crystalline sample mounts onto a manipulator with thermocouple sensors for temperature control. The heating-cooling stage operates with both radiant and electron bombardment heating options and with a closed-cycle helium refrigerator, giving a temperature range from ~ 60 K to 1200 K. Also available in the scattering chamber are a sputter source, gas doser, and residual gas analyzer. The four differential pumping stages constituting the TOF section link the scattering chamber to the detector chamber, which is maintained at pressures in the high 10^{-11} mbar range. (See Fig. 1.) This chamber houses the electric quadrupole mass spectrometer, its associated electron bombardment ionizer, and channeltron electron multiplier.⁴¹ The helium atom background signal is minimized by the attached sump chamber which is designed to pump away nonionized helium atoms that would otherwise pass through the mass spectrometer and then reflect back into the ionizer. The pulses from the channeltron electron multiplier due to the arrival of single ionized He atoms are fed into a CAMAC interface and then stored in a PC computer. Almost the entire operation of measurement is automated under computer control through LABVIEW (Ref. 42) software. With this technology the HAS instrument can be preprogrammed for a set of experiments and partial remote control can be employed.

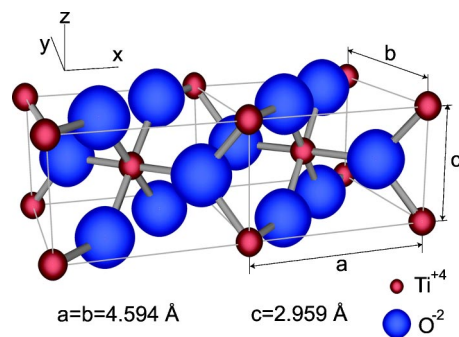


FIG. 2. Bulk structure of TiO_2 showing two unit cells and the a , b , and c lattice constants.

A. Sample preparation

1. Bulk TiO_2 unit cell and the (110) surface unit cell

The bulk structure of rutile TiO_2 , Fig. 2, consists of tetragonal unit cells with two TiO_2 units per cell. Each Ti^{4+} ion is sixfold coordinated with neighboring O^{2-} ions, and each O^{2-} ion is surrounded by three Ti^{4+} ions.^{43,44} The $5 \times 5 \times 1 \text{ mm}^3$ samples were obtained in cut and polished form from Commercial Crystal Laboratories, Inc.⁴⁵ A ball-and-stick model of the ideal (110) surface is illustrated in Fig. 3 where the surface titanium and oxygen ions are shown at their bulk positions.^{46,47} The surface titanium ions are either fivefold or sixfold coordinated whereas the surface oxygen ions are located both at in-plane threefold-coordinated sites and at protruding twofold-coordinated sites. The adjacent “bridging” oxygen rows are elevated by 1.2 \AA and separated by 6.495 \AA , as shown by a_1 in Fig. 3. The distance⁴⁴ between the bridging oxygens is 2.959 \AA , a_2 in Fig. 3 (also the c cell dimension in Fig. 2).

Figure 3 also reveals the rectangular surface net for the (110) surface, which is shown more explicitly in the direct lattice points of Fig. 4(a). Figure 4(b) presents the corresponding surface reciprocal lattice with the first SBZ (Ref. 48) and its special points $\bar{\Gamma}$, \bar{X} , \bar{Y} , and \bar{S} , labeled following the notation of Pelg *et al.*³⁰ Note that there are two high-symmetry directions perpendicular to each other, $\bar{\Gamma X}$ and $\bar{\Gamma Y}$, and that the SBZ diagonal $\bar{\Gamma S}$ corresponds to scattering from the planes indicated by the dashed lines in Fig. 4(a). The repeat rods in the reciprocal-space plot are labeled accordingly.

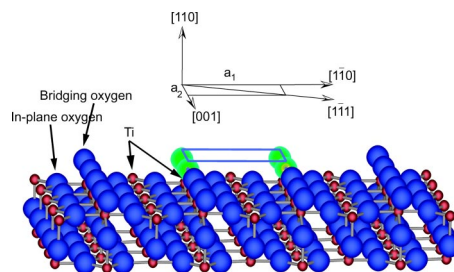


FIG. 3. Ball-and-stick model of the ideal (110) surface of rutile TiO_2 . The surface unit cell is shown by the light-shaded balls and the bulk lattice directions of the surface cell constants are indicated.

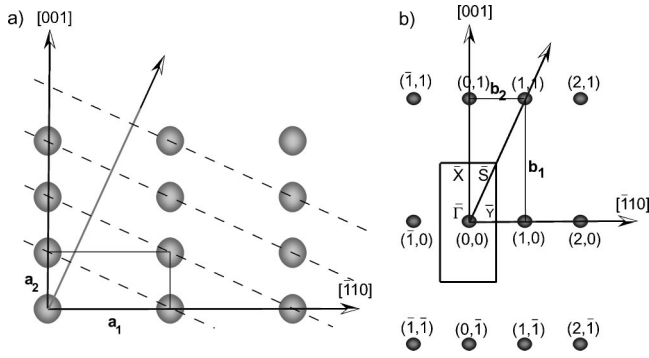


FIG. 4. The direct lattice (a) and reciprocal lattice (b) for the rutile TiO_2 (110) surface. In (a), solid lines outline the surface unit cell; dashed lines indicate scattering planes in the $\bar{\Gamma}\bar{S}$ direction. In (b), the reciprocal-lattice points are labeled as multiples of the unit surface reciprocal-space lengths and the SBZ is outlined with its special points $\bar{\Gamma}$, \bar{X} , \bar{Y} , and \bar{S} indicated. The azimuthal directions are given with respect to the bulk lattice directions.

2. Sample treatment

The cut and polished targets required multiple cycles of sputtering (0.5 kV Ar^+ for 20 min at 4 μA) followed by 20 min of annealing at 900 K, in accordance with a well-established preparation technique for rutile TiO_2 (110).^{43,49} As obtained from the vendor, the samples appeared transparent tan in color. However, with increased oxygen vacancies caused by the annealing, they became sequentially yellow, light blue, dark blue, and, finally, nearly black. This treatment and aging ultimately leads to the formation of crystallographic shear planes,⁵⁰ a common occurrence for TiO_2 , which tends to affect the scattering intensity adversely. The experiments reported in this paper were carried out on targets which manifested no significant crystallographic shear effects in the helium atom diffraction experiments discussed in the next section. Further, the samples were never heated sufficiently to induce the reported (1×2) reconstruction.³¹

In separate studies, we found that we could recover the initial crystal color by annealing our dark samples in a furnace at 1370 K for about 26 h at atmospheric oxygen pressure.⁵¹ Similar annealing of blue or black samples in the scattering chamber in a background of oxygen ($\sim 10^{-6}$ mbar) had no effect on either the color or the scattering intensities. Additionally, we observed that when previously well-characterized samples were exposed to air and then reinstalled in the scattering chamber, the targets required a somewhat vigorous treatment to restore the diffraction intensities to their previous values: namely, heating at temperatures near 1120 K for about 10 min.

B. Typical measurements: Angular distributions and time-of-flight spectra

1. Elastic scattering

Angular distribution (AD) experiments^{11,39} were performed to determine the helium atom diffraction pattern from the surface. These are carried out by measuring the scattered

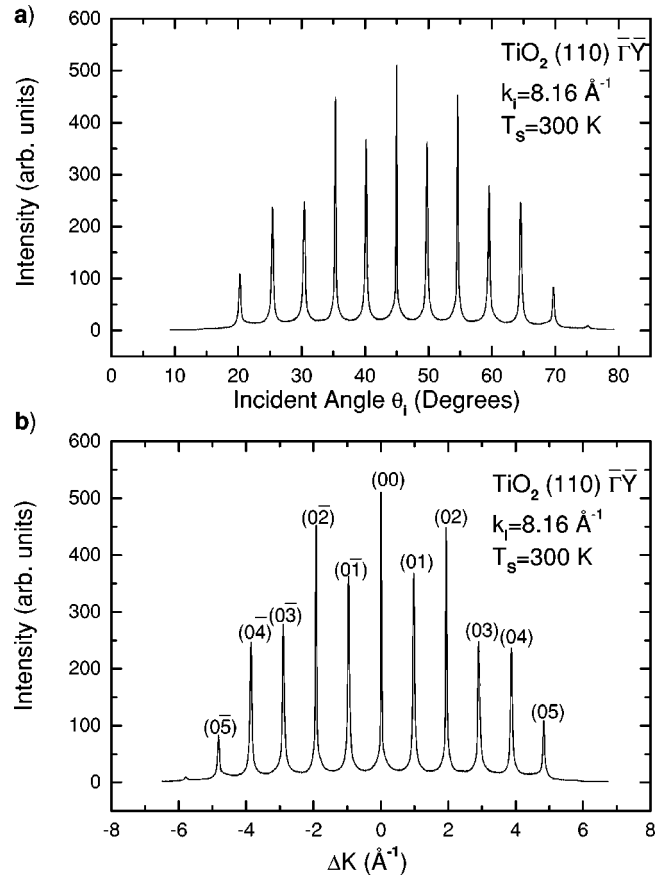


FIG. 5. A typical angular distribution (AD) for rutile TiO_2 (110) in the $\bar{\Gamma}\bar{Y}$ azimuth with surface temperature $T_s = 300$ K. The upper panel (a) shows the data as taken in the laboratory as a function of incident angle θ_i . In the lower panel (b) the abscissa has been converted into parallel momentum transfer ΔK , as indicated in the text. The central peak, at 45° in the upper panel and at $\Delta K = 0$ in the lower panel, is the specular reflection with symmetric Bragg peaks flanking either side. The labels on the peaks in the lower panel are the (n, m) indices of the surface reciprocal-lattice vector $G_{n, m}$.

atom intensity as a function of the incident angle θ_i with the chopper translated out of the beam line. (See Fig. 1.) In this instrument, with the total source-target-detector angle fixed to be 90° , the scattered atoms are always observed at angle $\theta_f = 90^\circ - \theta_i$. (See Fig. 1.) The measured intensities are then treated as a function of the parallel momentum transfer, ΔK , which is defined as $\Delta K = k_f \sin \theta_f - k_i \sin \theta_i$, where k_f and k_i are the final and initial helium atom wave vectors, respectively. For elastic scattering in AD measurements, $k_f = k_i$ so that $\Delta K = k_i (\cos \theta_i - \sin \theta_i)$. The Bragg condition for diffraction is that $\Delta K = G_{n, m}$, where $G_{n, m}$ is a surface reciprocal-lattice vector.^{4,11,39} Hence, in AD's the diffraction peaks in the atom scattering intensity are expected at angles for which this condition is satisfied. An example is shown in Fig. 5. The positions of the diffraction peaks in an AD give the values of the $G_{n, m}$ and thereby the surface lattice spacing; the diffraction peak intensities are related to the corrugation of the surface electronic densities.^{1,4}

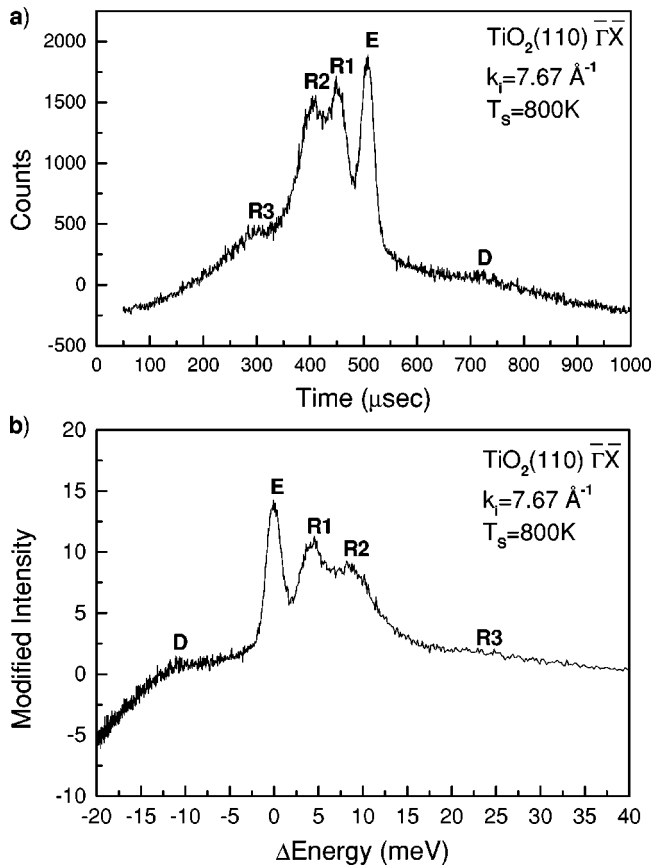


FIG. 6. (a) Measured TOF signals from $\text{TiO}_2(110)$ in the $\overline{\Gamma X}$ azimuth showing several peaks. **R1**, **R2**, and **R3** are surface phonon modes, **E** is the diffuse elastic peak, and **D** is a deception (Refs. 11, 55, and 56). (b) Arrival times in (a) have been converted to energy transfer; positive energies correspond to phonon annihilation scattering events and negative energies to creation events.

2. Inelastic scattering

To measure the inelastic helium scattering with the TOF technique, the chopper is retained in the beam line.^{11,39} (See Fig. 1.) The experimental conditions can be controlled so that single-phonon annihilation and creation events yield intensities sufficient to produce well defined peaks in the TOF spectra in acquisition times of one-half hour to an hour. For phonon annihilation events the helium atoms gain energy and arrive before the elastically scattered atoms from the same pulse, whereas for the creation events the atoms arrive after the elastically scattered atoms. The arrival times at the peak positions can be converted through energy conservation to the phonon energies $\hbar\omega$ and from parallel momentum conservation to the surface components of the phonon wave vectors, Q . Namely, $\hbar\omega = E_f - E_i$ and $\Delta K = k_f \cos \theta_i - k_i \sin \theta_i = G_{n,m} + Q$.^{11,39} A typical TOF spectrum is shown in Fig. 6(a). Figure 6(b) shows the same spectrum with arrival times converted to atom energy gain ($\hbar\omega > 0$) and loss ($\hbar\omega < 0$). TOF spectra taken over a range of incident angles and azimuths allow the determination of the phonon energies and corresponding wave vectors for mapping out the phonon dispersion curves, $\omega(Q)$, of the surface.^{11,37,39} (See the discussion in Sec. IV.)

III. ANGULAR DISTRIBUTIONS AND THE DEBYE-WALLER EFFECT

The (1×1) diffraction pattern expected for the stoichiometric (110) surface was observed in low-energy electron diffraction (LEED) experiments⁴⁶ and has now been recorded in HAS AD's for the $\overline{\Gamma X}$, $\overline{\Gamma S}$, and $\overline{\Gamma Y}$ SBZ directions over the range of surface temperatures from ~ 100 K to 1000 K. Figure 5 is the AD for the $\overline{\Gamma Y}$ direction at a surface temperature of 300 K. The diffraction patterns differ over this wide range of temperatures only in that the widths of the diffraction peaks tend to increase as the surface temperature increases; the peak positions remain at the same ΔK values, verifying that the lattice parameters of the surface unit cell have not changed to within our experimental resolution ($\approx 1\%$). Since the FWHM of diffraction peaks is inversely related to the size of the scattering domains, the increase in the widths with increasing T_s suggests that the terraces decrease in area as the temperature increases. However, some of this increase in width may be attributed to the Debye-Waller effect which is responsible for the marked decrease in diffraction intensities with increasing surface temperature.

Several reconstructions have been noted in other studies of this surface. In this work, we were able to obtain evidence for the (4×1) step-edge reconstruction⁴⁷ in the $\overline{\Gamma X}$ direction on only two targets as shown in the AD's of Figs. 7(a) and 7(b), where several, low-intensity, quarter-order peaks can be seen. The AD of Fig. 7(a) was obtained, in fact, for a sample still undergoing the surface preparation protocol described above, which accounts for the relatively large background signal. After the preparation procedure on this target was completed, the quarter-order diffraction peaks were no longer to be found. The apparent elusive nature of this reconstructed structure in these experiments may reflect the small surface area of the (4×1) -ordered domains even though they may be present in sufficient numbers to be found and imaged by STM. The very small and relatively broad two-fourths-order peaks in Fig. 7(b), particularly, suggest that only a very small fraction of the (110) surface has this structural feature.

According to the Debye-Waller effect, the specular intensity should fall off approximately exponentially with increasing temperature.⁵² A plot showing this for data in the $\overline{\Gamma X}$ direction is displayed in Fig. 8. From the slope of the straight-line portion, -0.0031 K^{-1} , one can calculate the surface Debye temperature if the mass of the helium atom scatterer at the surface is known. Whereas no ambiguity exists for materials such as metals with a single atom per unit cell, in this case the unit cell is composed of six ions and the mass of the scatterer is somewhat uncertain. We have arbitrarily chosen this mass to be 80 g/mol, corresponding to the total mass of a TiO_2 unit, which then gives the surface Debye temperature, $\Theta_D = 310 \text{ K}$.⁵² Since the Debye temperature and the scatterer mass are inversely proportional, the value obtained here can easily be corrected when a better choice for the mass is identified. The Debye-Waller exponent is a measure of the average number of phonons exchanged in the atom/surface scattering event at a given surface temperature⁵³ T_s : namely, $\langle n \rangle \approx T_s / \Theta_D$. The value obtained

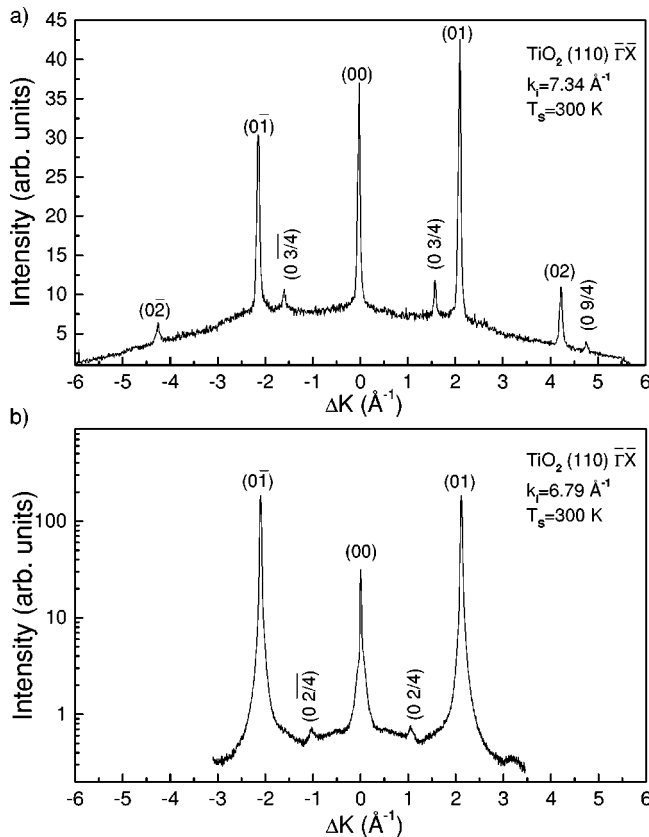


FIG. 7. Two examples of (4×1) step-edge reconstruction of the (110) surface of TiO_2 in the $\Gamma\bar{X}$ direction. (a) Three-fourth- and (b) two-fourth-order peaks in the AD's indicate a periodicity-4 times the surface unit cell in this direction. The background signal in panel (a) is relatively large because the surface preparation of this sample had not been completed, as described in the text. Note that the ordinate scale in the panel (b) is logarithmic in order to exaggerate the size of the quarter-order peaks.

here for Θ_D is roughly consistent with the multiphonon scattering observed in the TOF experiments described in the next section.

IV. SURFACE DYNAMICS OF RUTILE $\text{TiO}_2(110)$

A. Discussion of time-of-flight measurements

The principal focus of this investigation is the determination of surface phonon dispersion curves in the high-symmetry azimuths of the SBZ as a function of surface temperature. HAS is unique in permitting experiments on the surface dynamics of crystals to be carried out in the same instrument as measurements of the surface structure.

Bishop *et al.*⁵⁴ have described the main features observed in TOF spectra for scattered helium atoms and the physical processes that cause them. The coherent elastic scattering, usually recorded in AD's as specular and Bragg diffraction peaks, and Debye-Waller temperature-dependent effects⁵² have already been discussed above. Others effects include (a) the incoherent elastic scattering, also called diffuse elastic scattering, that arises from surface defects and appears at the elastic arrival time in TOF spectra (peaks labeled 1 in Fig. 9

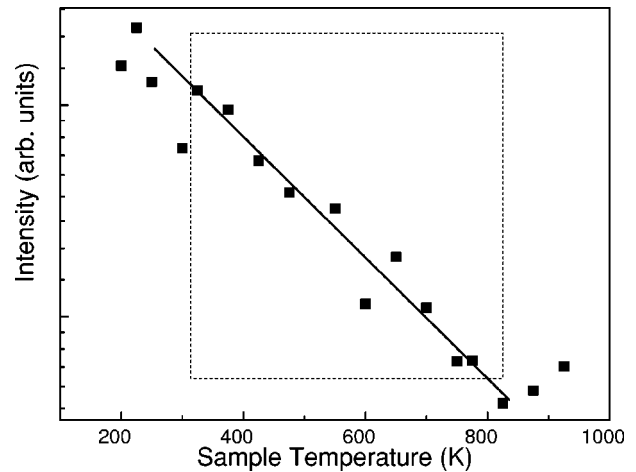


FIG. 8. Semilog plot of specular intensity in the $\Gamma\bar{X}$ direction as a function of sample temperature. Dashed box indicates the boundaries of the fitted data.

below); (b) artifacts called deceptons^{11,55,56} (labeled 2); (c) the diffuse inelastic scattering that appears as a broad “foot” in the TOF spectra and includes both incoherent inelastic scattering from defects and coherent multiphonon scattering⁵⁷ (labeled 3); and (d) coherent single-phonon inelastic scattering, which one uses to calculate the surface dispersion curves (labeled 4).

Although the diffuse elastic peaks labeled 1 which appear at $\Delta E = 0.0$ meV might seem to be in the way, they are actually of use in the analysis of the data because they mark the elastic arrival times. One should note, moreover, that in this work the intensities of the diffuse elastic peaks are rather large, which indicates that the surface contains a substantial number of defects including steps. The deceptons shown in peaks labeled 2 would be nuisances if they were not so easily identified and removed in the analysis.^{11,55,56}

Using the theoretical methods developed for the analysis of multiphonon scattering,^{54,57} one can, in principle, compute the multiphonon contribution [noted in item (c) above] to the scattering intensity in the TOF spectra and subtract it from the background. However, for most of the measurements that were carried out, this contribution can be ignored and the peaks properly identified. This is fortunate since the value obtained above for the surface Debye temperature is highly uncertain and the computational effort required to correct for the multiphonon contribution did not seem to be worthwhile. In the few high-temperature experiments where the multiphonon scattering did appear to interfere with evaluating the energy and momentum transfer from a single-phonon TOF peak (see below), the resulting datum was excluded in the determination of the surface phonon dispersion.

The construction of the surface phonon dispersion curves from the TOF spectra requires calculation of the phonon energies and wave vectors, as indicated in Sec. II, from the single-phonon TOF peaks (labeled 4). However, several impediments to straightforward evaluation of the data sometimes arise which can lead to low confidence in the results. Foremost among these is the imprecision in determining the phonon energy when the energy transfer is small. This is

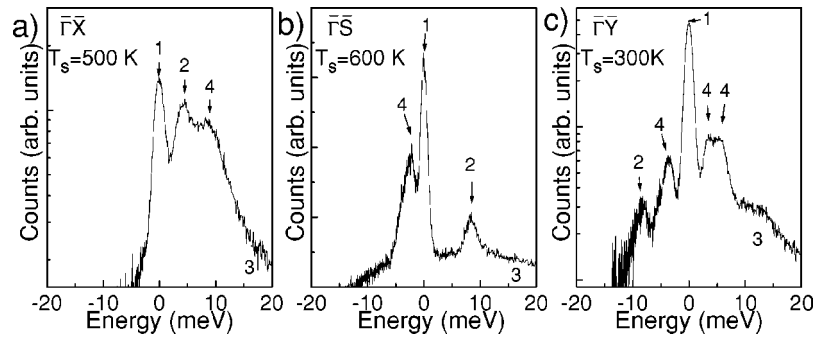


FIG. 9. Illustrative TOF spectra converted to energy transfer spectra, in the three high-symmetry directions: (a) $\bar{\Gamma X}$, (b) $\bar{\Gamma S}$, and (c) $\bar{\Gamma Y}$. Peaks are labeled as follows: 1, incoherent elastic; 2, deception; 3, diffuse inelastic; 4, single-phonon scattering.

because the uncertainty in locating the peak position is, approximately, independent of the phonon energy. Hence, the relative errors are larger for low-energy phonons and often lead to significant scatter in the calculated dispersion curves.

Another problem arises when two single-phonon TOF peaks lie close to each other in arrival time, or even merge, because of the way the scan curve intersects the dispersion curve under the conditions of the experiment.^{11,37,39} For such merged peaks, small uncertainties in time can lead to large errors in energy and momentum transfer. In many cases we have tried to resolve the merged peaks by repeating the experiment under modified scattering conditions, usually with smaller incident helium wave vectors (and incident energy). However, this was not always successful and often not possible. To reduce the scatter in the calculated dispersion curves due to this effect, we have simply not included data points in the dispersion curve wherever they could not be sufficiently resolved (see also Sec. IV C). A related problem that occurs in a few TOF spectra taken at high temperatures is the merging of large multiphonon peaks with single-phonon peaks. These data have also been left out of the measured dispersion curves. Both of these effects seem to occur mainly, but not entirely, on the annihilation side of the TOF spectra. Thus, many of the extended SBZ plots presented below consist almost entirely of single-phonon creation TOF data.

Over 6500 TOF spectra were taken on three samples of rutile TiO_2 in the $\bar{\Gamma X}$, $\bar{\Gamma S}$, and $\bar{\Gamma Y}$ directions. The incident wave vectors used in these investigations ranged from 6.74 to 9.23 \AA^{-1} and the surface temperatures ranged from 150 K to 1000 K. We note that the scattering intensities in these directions were found to vary substantially from target to target and therefore some of the dispersion curves presented below have greater scatter than others. We believe that this variation may be due to the sensitivity of the surface to the preparation protocol.

After the experiments had been carried out on the three original samples, a fourth sample was obtained. This sample proved to have an exceptional surface in the $\bar{\Gamma X}$ direction, yielding specular peak counting rates of approximately 2 MHz, approximately double those of the original samples. This high intensity permitted substantial improvements in the signal to noise. However, the scattering intensities in the $\bar{\Gamma Y}$ direction were, disappointingly, much weaker.

The results of the surface phonon measurements are presented below in three different ways. First, the measured surface phonon dispersion curves are displayed for each surface temperature for each SBZ direction. Then, to determine the character of the observed vibrational modes, the intensities of surface phonon TOF peaks in each direction are plotted as a function of surface phonon wave vector and, in addition, comparisons are made with calculations for rutile MgF_2 (110). Finally, to illustrate that the surface undergoes structural modification at low temperatures, the surface phonon energies extrapolated to the SBZ center for each direction are plotted as a function of surface temperature.

B. Determining the polarization of the observed rutile TiO_2 (110) vibrational modes

The scattering intensities of the single-phonon creation and annihilation events vary approximately with $\langle \Delta \mathbf{k} \cdot \mathbf{u} \rangle^2$, where $\Delta \mathbf{k}$ is the resultant wave vector of the scattered helium atom and \mathbf{u} is the vibrational displacement vector due to the phonon.⁵³ At the specular reflection angle, the parallel component of $\Delta \mathbf{k}$ is at its smallest ($\Delta K = 0$) and the perpendicular component Δk_z is at its maximum. Thus, in principle, as one goes across the SBZ, from zone center to zone boundary, the relative intensities of the phonon peaks should increase for longitudinally polarized phonons and decrease for phonons polarized perpendicular to the surface.^{58,59} In practice, the surface phonons are generally elliptically polarized in the sagittal plane, with both surface parallel and perpendicular components. Nevertheless, some indication of the dominant polarization can be obtained by plotting the relative phonon intensities against ΔK . One should note, however, that under our experimental conditions ΔK is usually much smaller than Δk_z .

Comparison of the measured phonon dispersion with model calculations usually provides the surest identification of the phonon mode polarizations. In this case, since the TiO_2 (110) surface has not yet been studied theoretically, we rely for some guidance in interpreting the phonon intensity plots above on the surface dynamics calculations reported for rutile MgF_2 (110).³⁰ For many materials, including the rock-salt metal oxides, similarities in structure usually result in similarities in the character of the vibrational modes. At the most elementary level, for example, analysis of the dynamic

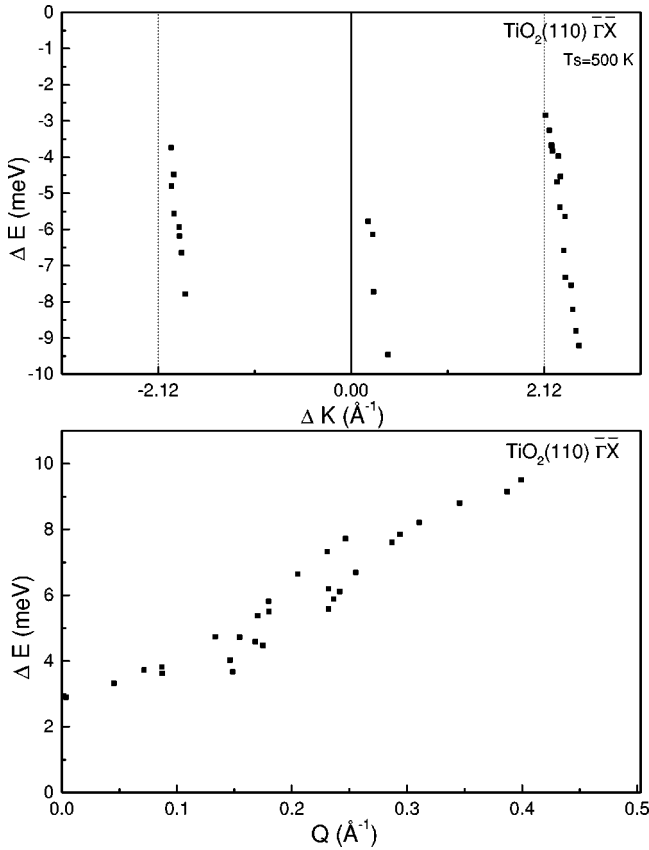


FIG. 10. Surface phonon dispersion curves for rutile TiO_2 (110) in the $\overline{\Gamma X}$ azimuth at $T_s = 500$ K. The upper panel presents the data in an extended SBZ plot; the lower panel shows the same data in a reduced SBZ plot. The reciprocal lattice points $G_{0,1} = 2.12 \text{ \AA}^{-1}$ and $G_{0,\overline{1}} = -2.12 \text{ \AA}^{-1}$ and the boundaries of the first SBZ are at $\pm 1.06 \text{ \AA}^{-1}$. Note in the lower panel that the data extend only to about 40% of the SBZ boundary.

behavior of a simple diatomic chain shows that the character of the vibrational modes is largely independent of the force constants and atomic masses, even though the energies of the phonon branches vary with these parameters.^{57,60} This same concept, based on a shell model calculation of the bulk lattice dynamics of TiO_2 ,²⁹ was used to model several compounds having the bulk rutile structure: GeO_2 , SnO_2 , NbO_2 , and VO_2 . Thus, we expect that if MgF_2 (110) has a surface-localized vibrational mode or resonance in a high-symmetry azimuth of the SBZ with a certain polarization that TiO_2 (110) ought to have a similar mode or resonance in that high-symmetry azimuth of its SBZ.

C. Dispersion along $\overline{\Gamma X}$

Figures 10 and 11 present the dispersion curves measured at 500 K and 1000 K in the $\overline{\Gamma X}$ azimuth, the direction along the oxygen rows. (See Figs. 3 and 4.) These curves are part of a series of experiments carried out in this azimuth for surface temperatures of 200, 300, 500, 650, 800, and 1000 K. It is worth noting that although the Bragg peaks in the ADs at target temperatures of 1000 K were not as narrow as the ones at 300 K, the TOF spectra yielded more intense and better resolved peaks at the higher temperature.

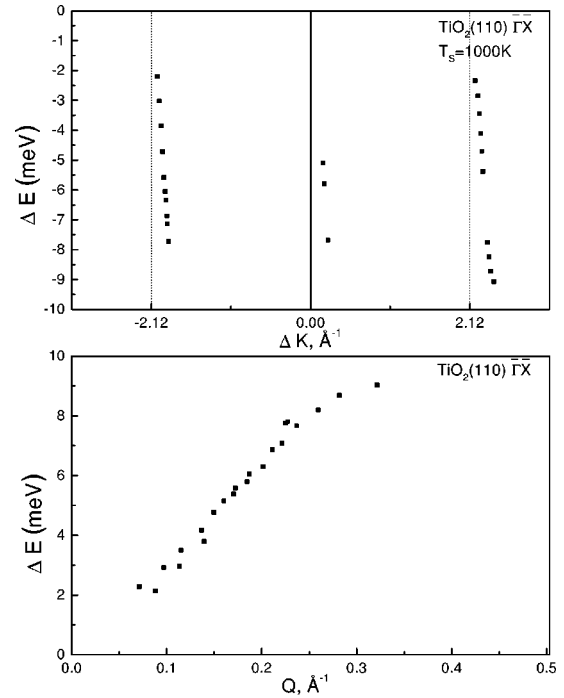


FIG. 11. Surface phonon dispersion curves for rutile TiO_2 (110) in the $\overline{\Gamma X}$ azimuth at $T_s = 1000$ K. The upper panel presents the data in an extended SBZ plot; the lower panel shows the same data in a reduced SBZ plot. The reciprocal lattice points $G_{0,1} = 2.12 \text{ \AA}^{-1}$ and $G_{0,\overline{1}} = -2.12 \text{ \AA}^{-1}$ and the boundaries of the first SBZ are at $\pm 1.06 \text{ \AA}^{-1}$. Note in the lower panel that the data extend only to about 40% of the SBZ boundary.

Figure 12 displays an extended zone plot at $T_s = 300$ K, which contains, in addition to the data, scan curves¹¹ for incident angles of 27° , 28° , 30° , 36.5° , and 37.5° . We examined this case in great detail with the fourth rutile sample in order to understand the problem of resolving merged peaks which was noted above. The TOF spectra converted to energy transfer spectra for the five angles are given in Fig. 13. The spectrum in Fig. 13(a) taken at an angle of 27° reveals two nearly resolved creation peaks and a very weak broad peak on the annihilation side. The two creation events give rise to two energy-momentum transfer points that lie on the 27° scan curve in Fig. 12. The annihilation peak is observed more clearly in the original TOF spectrum. The Jacobian of the transformation from time to energy transfer broadens the peak, as observed in Fig. 13(a), and makes it difficult to determine the peak's position. This uncertainty in peak position is evident on the annihilation side for this angle; a similar difficulty occurs for other peaks in this region of the SBZ. In Fig. 13(b) for the angle 28° , the two creation peaks have merged closer together and are more difficult to resolve. In the next panel, Fig. 13(c), for 30° , the peaks have merged further and moved close to the diffuse elastic peak at the SBZ center. The other, clearly defined peak on the creation side (D) is a decepton.^{55,56}

The behavior of the creation-side single-phonon peaks in these three panels can be understood by observing how the scan curves intersect the dispersion curve, represented here by the heavy dark line in Fig. 12. We note that the scan curve

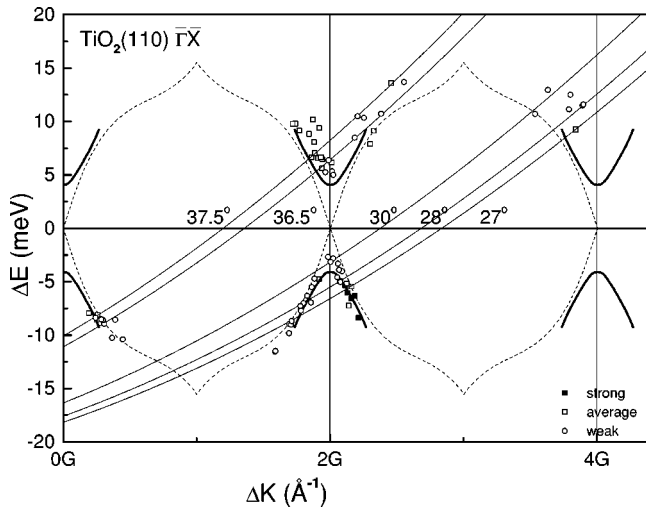


FIG. 12. Extended SBZ phonon dispersion curves for rutile TiO_2 (110) in the $\overline{\Gamma X}$ azimuth at $T_s = 300$ K. Five different scan curves (solid lines) are shown for TOF experiments at the five incident angles labeled. The heavy solid line is the approximate form of the dispersion curve inferred from data accumulated at similar scan curves from a large number of incident angles. The dashed curve is a bulk transverse acoustic dispersion curve taken from Traylor *et al.* (Ref. 26). Different symbols for the data points represent the certainty of the points and are indicated in the legend in the figure. The abscissa scale symbol G stands for a reciprocal-lattice unit $= 2.12 \text{ \AA}^{-1}$. The SBZ boundaries are at odd multiples of $G/2$.

at a particular angle represents the constraints of energy and momentum conservation for the scattering of helium atoms which create or annihilate single surface phonons.^{11,37,39} A surface phonon can exchange energy and momentum at the point where the phonon dispersion branch intersects the scan curve, thus providing a single-phonon peak in the TOF spectrum. The single-phonon peaks in a set of TOF spectra enable one to map out the dispersion branch by plotting the energy-momentum transfer points. From the data points obtained in this set of measurements, we have inferred the dispersion curve to lie near where the heavy dark line has been drawn in the figure. The curve repeats for each zone as shown.

It is clear from Fig. 12 that at an incident angle of 27° the scan curve passes through the dispersion curve in two places near $\Delta K = 1 G$ on the creation side (negative energy transfers) and that these two points should be resolvable. However, for the 28° -scan curve, the intersection points lie closer together, and at 30° they are closer yet. Furthermore, as indicated in Fig. 13, the intersection points should move nearer to the zone center as the incident angle is increased.

The spectrum in Fig. 13(e) for the incident angle 37.5° shows four clearly resolved peaks, two on the annihilation side and two on the creation side. (Only three of these lie on the scan curve of Fig. 12; the peak at $\Delta E \approx -13$ meV lies off the left-hand side of the figure.) Again, it is apparent from the intersections of the scan curve with the heavy dark line why they are resolvable. Moving to incident angle 36.5° , however, gives a merged double peak that is difficult to re-

solve. In this case, the peak located on the creation side is quite broad and of poor quality, and has therefore been omitted from Fig. 12. From the perspective of the intersections of the scan curves with the experimental dispersion curve in Fig. 12, one would not expect to observe single-phonon peaks in TOF spectra measured between incident angles of 30° to 35° , as we discovered in our experiments.

All of the results for the dispersion measurements in this azimuth are plotted in Fig. 14 including a representative error for each temperature measured. Two features become evident. First, the surface phonon dispersion curves for all surface temperatures extend only across about 40% of the SBZ from the zone center; the zone boundary lies at 1.06 \AA^{-1} . Second, although the data do not extend all the way to the zone center, the modes generally soften toward the zone center as the surface temperature is increased. This trend is illustrated in Fig. 15(a) where the phonon energies extrapolated to the SBZ center are plotted as a function of surface temperature. Along with this trend, the slopes (or stiffness of the vibrational modes) of the dispersion curves in Fig. 14 generally appear to increase as the temperature is increased.

As noted above, a decrease in surface phonon intensity with increasing parallel momentum transfer is generally characteristic of a vibrational mode polarized perpendicular to the surface.⁵⁸ Figure 16 for TOF experiments in the $\overline{\Gamma X}$ direction at 1000 K shows that the dispersive mode observed in this azimuth of the SBZ follows this behavior. However, one should bear in mind that the surface vibrational displacements observable by HAS can have both transverse and longitudinal components in the sagittal plane and that helium scattering is less sensitive to the longitudinal component because of the relative magnitudes of ΔK and Δk_z noted earlier. Thus, the very rapid drop-off in intensity away from the zone center in Fig. 16 may suggest that two effects are responsible. First, the intensity decreases as expected with increasing ΔK for the predominantly perpendicular vibrational displacements near the zone center; second, the character of the mode may be changing from mainly surface normal to mainly surface parallel as ΔK increases, which makes the vibration interact less with helium scattering. The change in polarization of this mode could be part of the reason that the single-phonon TOF data do not extend across the entire SBZ.

In their calculation for MgF_2 (110) in this azimuth, Pelg *et al.* do not indicate the presence of a low-energy, perpendicular surface vibrational mode in their Fig. 4, but they do show a surface resonance with longitudinal character.³⁰ On the other hand, their Fig. 5(a), which presents the calculated square amplitudes of the vibrational displacements, does show some density of states for the perpendicular vibration. However, for this displacement Pelg *et al.* note the likely hybridization of the surface vibrational mode with the surrounding bulk bands of the same symmetry. This picture, though sketchy, is consistent with our observations for TiO_2 (110): namely, that the polarization of the mode may be changing across the SBZ and, further, that the densities of states for both polarizations fall off with increasing ΔK as the result of hybridization with the bulk bands. Unfortu-

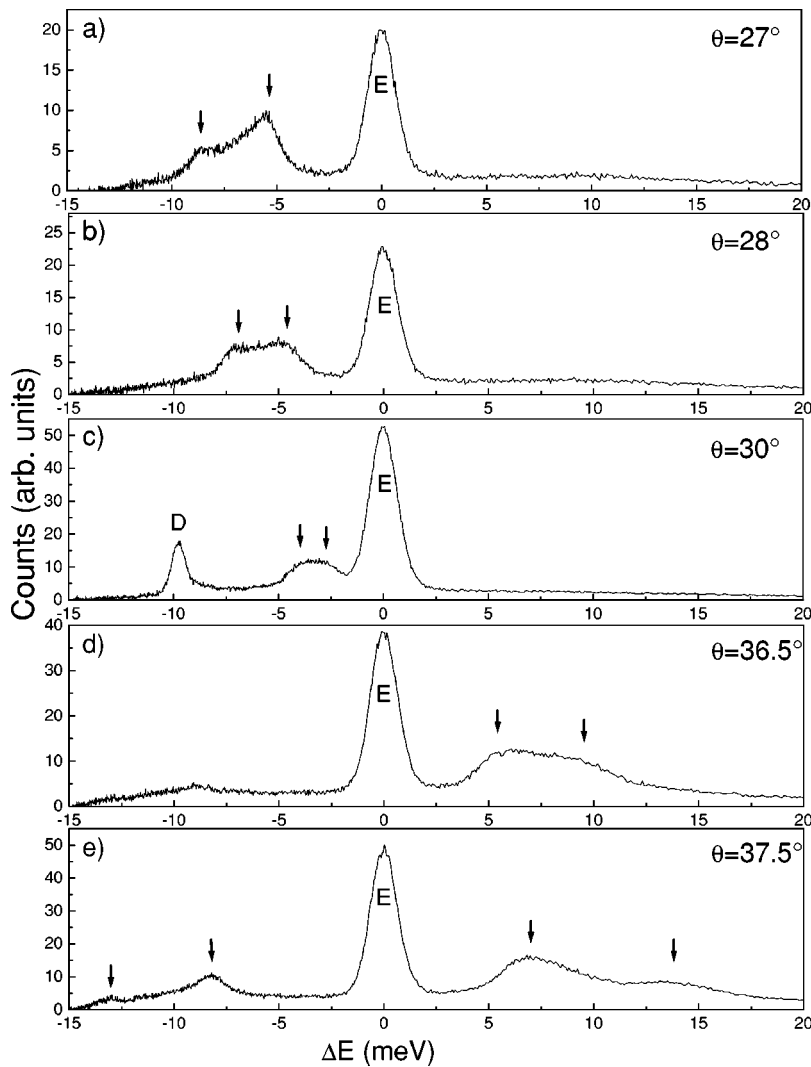


FIG. 13. Illustrative TOF spectra converted into energy exchange spectra for rutile TiO_2 (110) in the $\bar{\Gamma}\bar{X}$ azimuth. Incident beam wave vector $k_i = 6.79 \text{ \AA}^{-1}$. See text for details.

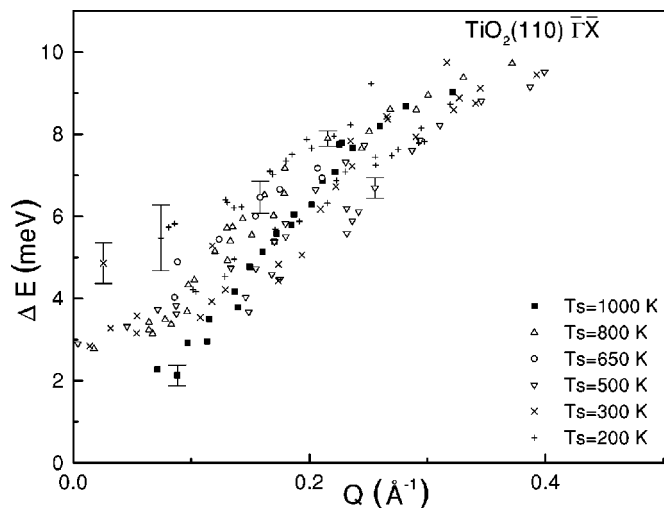


FIG. 14. Reduced SBZ phonon dispersion curves for rutile TiO_2 (110) in the $\bar{\Gamma}\bar{X}$ azimuth for all target temperatures measured. The temperatures associated with each symbol are identified in the legend in the figure. Note that the data extend only to about 40% of the first SBZ. Representative error bars are given for each of the surface temperatures studied.

nately, the report of these calculations for MgF_2 (110) does not provide information on which surface ions take part in this vibration.

Traylor *et al.* found a transverse acoustic mode in their neutron scattering experiments on bulk rutile TiO_2 that could be the origin of the surface mode observed here in the $\bar{\Gamma}\bar{X}$ direction.^{26,60} This mode, also measured at 300 K, is shown as the dashed curve in Fig. 12. It appears to match the inferred surface dispersion curve, shown in the figure as the heavy solid curve, in the region of the SBZ where we have been able to obtain TOF data. Theoretical modeling for this connection clearly needs much more work.

D. Dispersion along $\bar{\Gamma}\bar{S}$

Figure 17 presents the results of TOF measurements at a surface temperature of 450 K in the $\bar{\Gamma}\bar{S}$ azimuth, the direction along the SBZ diagonal. (See Fig. 4.) The figure shows a single-dispersion curve which appears to be a dispersive Rayleigh-like mode and is representative of the dispersion curves measured at surface temperatures of 200, 250, 300, 600, and 800 K. For comparisons, the measured dispersion curves for all the different surface temperatures are shown in

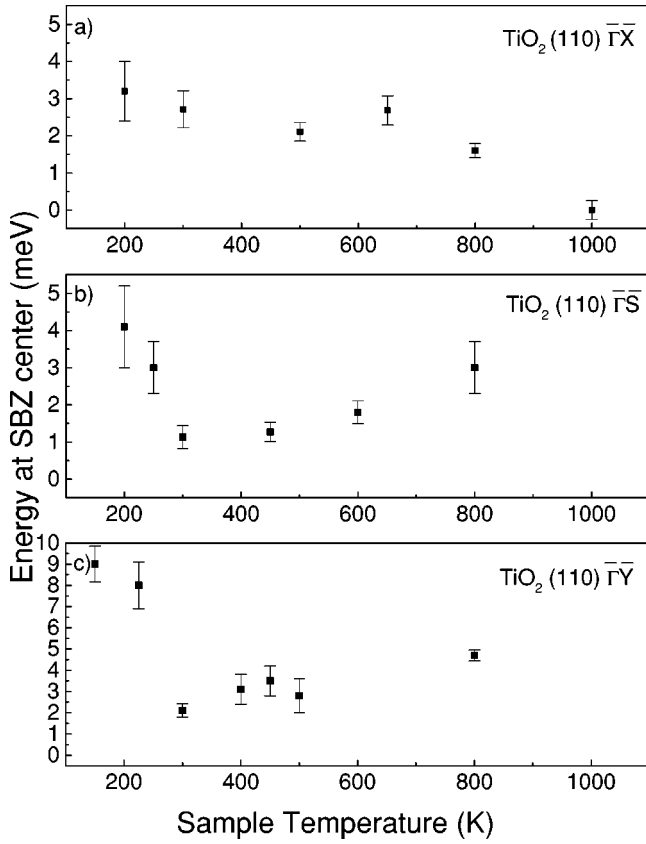


FIG. 15. Extrapolated surface phonon energies at the SBZ center, as a function of sample temperature, for three different directions. The error bars are derived from uncertainties in the peak locations in the TOF.

Fig. 18. With the exception of the very noisy data from the lowest-temperature measurement, all the dispersion points lie within about the 40% of the zone center, similar to the case with the results above in the ΓX azimuth.

The low-energy, perpendicularly polarized mode calculated by Pelg *et al.* for MgF_2 (110) in this azimuth has the characteristics of the Rayleigh wave. [See Fig. 4(a) of Pelg *et al.*] This low-energy, surface vibration is a macroscopic mode in that it penetrates into the crystal bulk to a depth proportional to the wavelength.³⁰ Interestingly, the calculations also show that there is a surface-localized longitudinal mode across most of the SBZ in this azimuth. For MgF_2 , the Rayleigh wave mainly involves the vibrations of the in-plane F^- ions, as shown in Fig. 1 of Pelg *et al.*, whereas the longitudinal vibration is mainly that of the bridging F^- ions. (See Fig. 3.) If this situation is similar for TiO_2 , as shown in Fig. 19, the O^{2-} ions taking part in the surface-normal vibration are likely to be screened somewhat from the scattering helium atoms by the bridging O^{2-} ions. Hence, the HAS measurements should reflect a trade-off between the high sensitivity of HAS for perpendicular vibrational displacements and the ability of the lattice to couple this motion to the helium atom probe.⁵⁸ The sharp falloff seen in Fig. 20 also suggests that for TiO_2 both of these surface modes may hybridize to some extent with the bulk vibrations away from the zone center. In any case, for a more quantitative com-

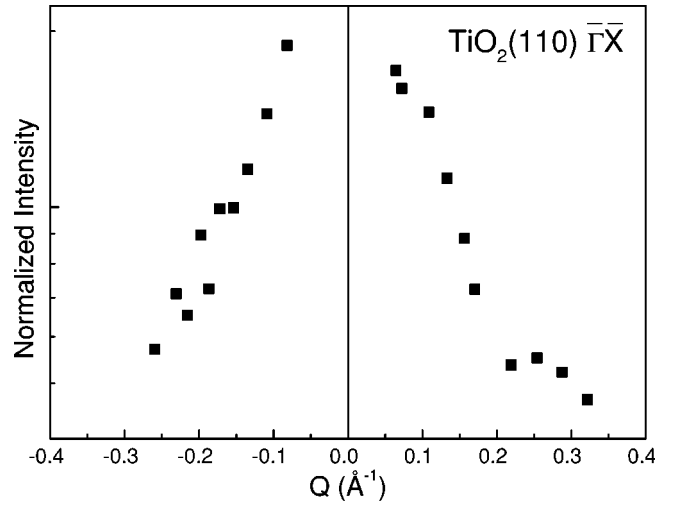


FIG. 16. Semilog plot of the relative surface phonon peak intensity vs parallel momentum transfer from the TOF data taken in the ΓX direction at 1000 K. The characteristic drop-off in intensity is indicative of a vibrational displacement polarized normal to the surface (Ref. 58). Note that only a representative sample of the data points have been included in this plot.

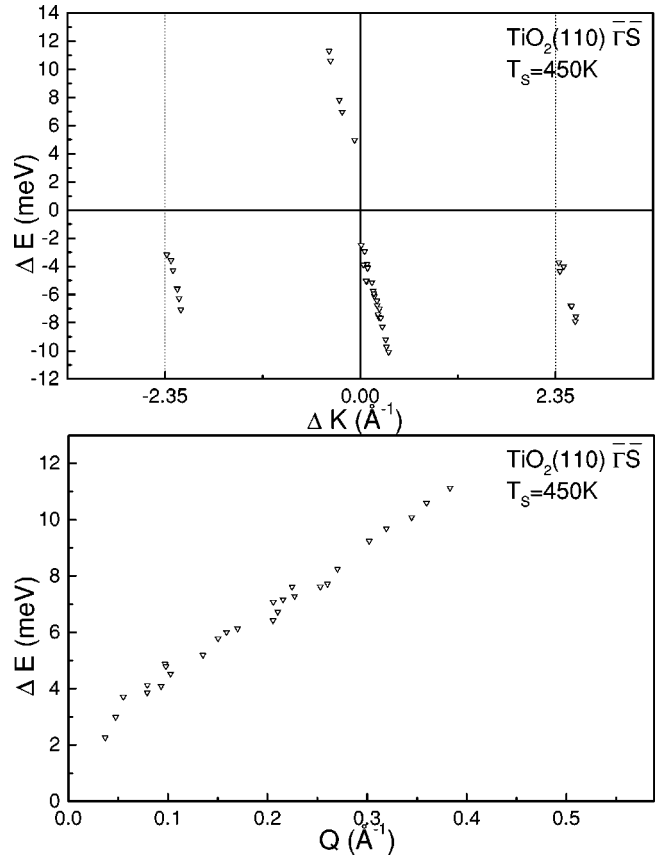


FIG. 17. Surface phonon dispersion curves for rutile TiO_2 (110) in the ΓS azimuth at $T_s = 450$ K. The upper panel presents the data in an extended SBZ plot; the lower panel shows the same data in a reduced SBZ plot. The reciprocal lattice points $G_{1,1} = 2.35 \text{ \AA}^{-1}$ and $G_{\bar{1},\bar{1}} = -2.35 \text{ \AA}^{-1}$ and the boundaries of the first SBZ are at $\pm 1.17 \text{ \AA}^{-1}$. Note in the lower panel that the data extend only to about 40% of the SBZ boundary.

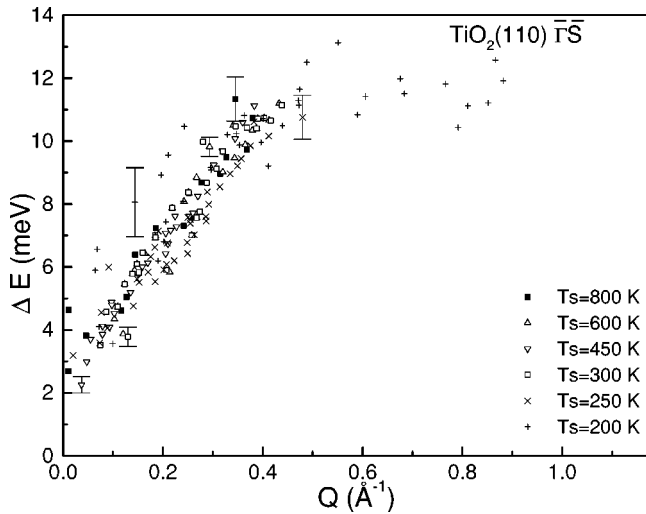


FIG. 18. Reduced SBZ phonon dispersion curves for rutile TiO_2 (110) in the $\bar{\Gamma}\bar{S}$ azimuth for all target temperatures measured. The temperatures associated with each symbol are identified in the legend in the figure. Note that the data extend only to about 35% of the first SBZ except for some scattered points from the 200 K experiment. Representative error bars are given for each of the substrate measurements.

parison to theory,⁵⁸ we would need to find an approximate potential model and use scattering theory for the comparison as given by Eichenauer *et al.*⁶¹ For the purpose of this work, the decrease in scattering intensity with increasing momentum transfer in Fig. 20 establishes that the observed mode is very likely the Rayleigh mode.

Unlike the behavior found in the $\bar{\Gamma}\bar{X}$ azimuth, the phonon energies extrapolated to the zone center in this direction were found first to soften, but then to stiffen with increasing temperature. These data are shown in Fig. 15(b).

E. Dispersion along $\bar{\Gamma}\bar{Y}$

Figure 21 shows two TOF spectra, converted to energy transfer spectra, obtained in the $\bar{\Gamma}\bar{Y}$ direction for substrate temperatures of 225 and 500 K. The difference in quality of these spectra—namely, the definition of the shapes of the peaks—is quite evident and typical of the improvement in signal to noise that was encountered in these studies as the surface temperature was raised. From TOF spectra similar to these, we have constructed the dispersion curves in this azimuth for the surface temperatures of 150 and 225 K that are

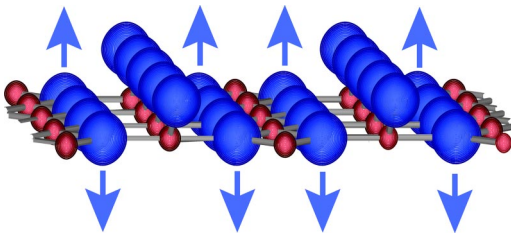


FIG. 19. Suggested ionic motion for the low-energy surface normal vibrations of TiO_2 in the $\bar{\Gamma}\bar{S}$ azimuth, based on Pelg *et al.*, where Ti and O are substituted for Mg and F, respectively.

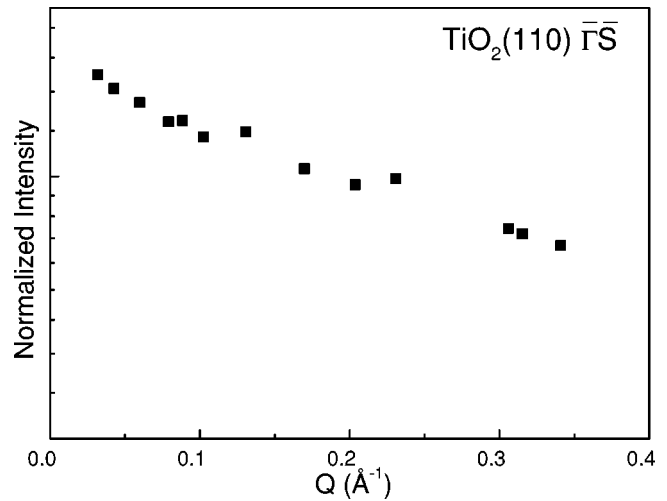


FIG. 20. Semilog plot of the relative surface phonon peak intensity vs momentum transfer from the TOF data taken in the $\bar{\Gamma}\bar{S}$ direction for a substrate temperature of 450 K. The characteristic drop-off in intensity is indicative of a vibrational displacement polarized normal to the surface (Ref. 58). Note that only a representative sample of the data points have been included in this plot.

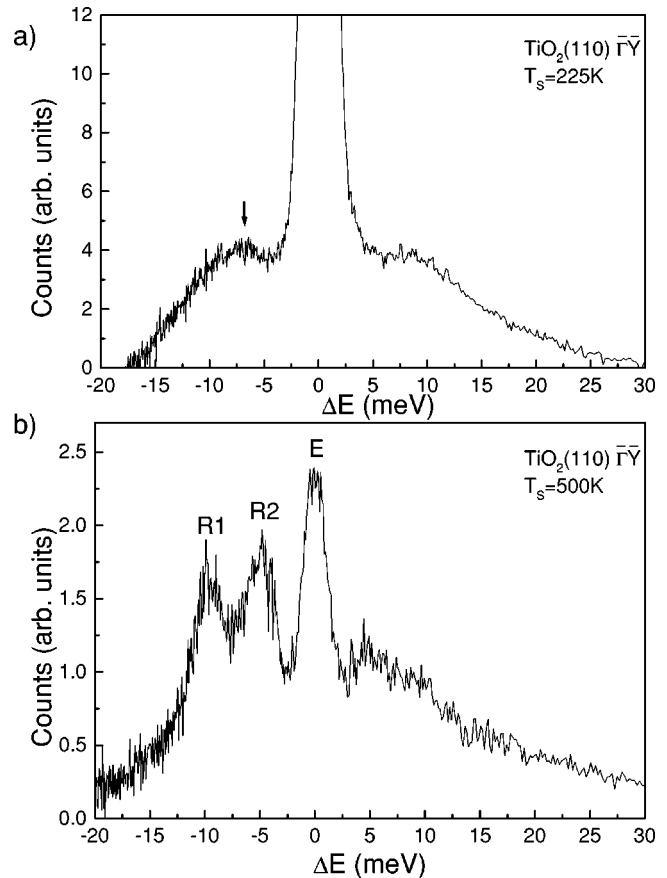


FIG. 21. Two TOF spectra in the $\bar{\Gamma}\bar{Y}$ azimuth, converted to energy transfer spectra for (a) $T_s=225$ K and (b) $T_s=500$ K. In (a) the broad, poorly defined single-phonon peak is indicated by an arrow. The relatively large peak at $\Delta E=0$ is the diffuse elastic peak. In (b) two single-phonon peaks, labeled R1 and R2, are clearly resolved. Note that the diffuse elastic peak, labeled E, is relatively much smaller than that in (a).

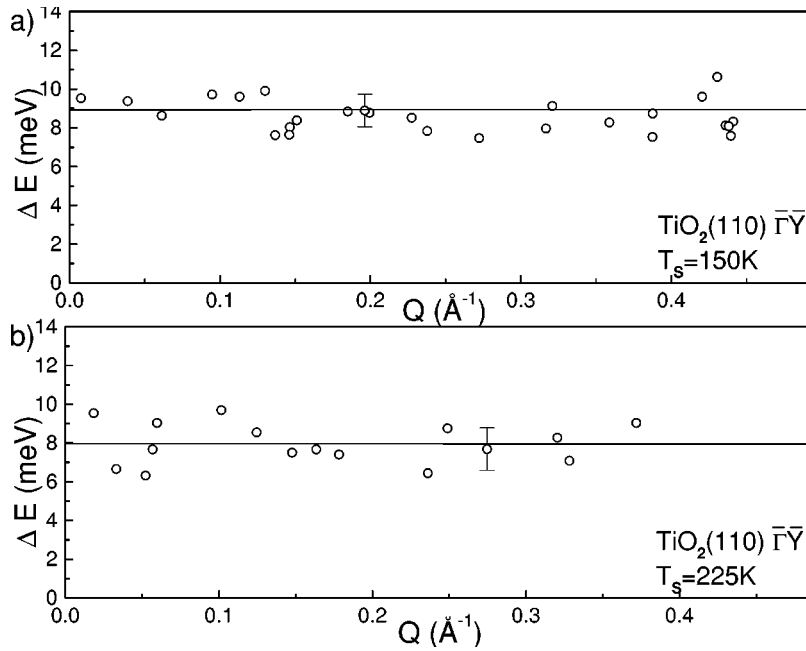


FIG. 22. Reduced zone surface phonon dispersion curves for rutile TiO_2 (110) in the $\bar{\Gamma}\bar{Y}$ azimuth at $T_s=150$ K (upper panel) and $=225$ K (lower panel). The boundaries of the first SBZ are at $\pm 0.48 \text{ \AA}^{-1}$. Note that the data extend to nearly 100% of the SBZ boundary. The horizontal straight lines in each panel are best fits to the data points. Representative errors are also shown.

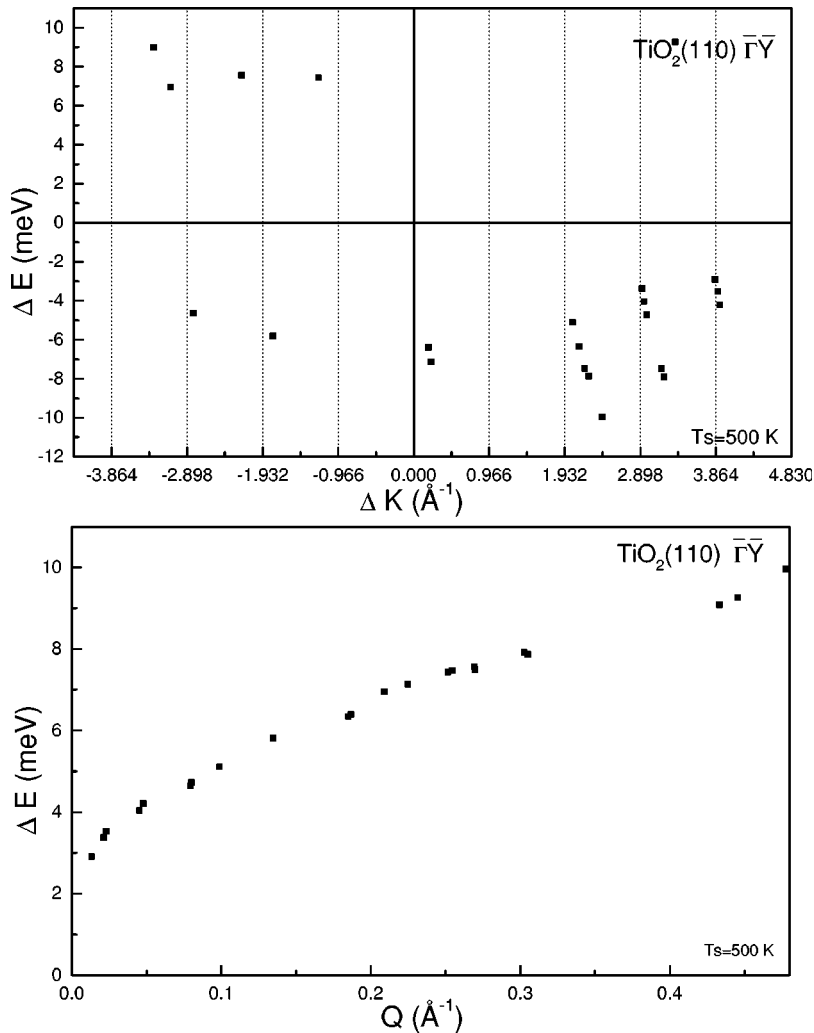


FIG. 23. Surface phonon dispersion curves for rutile TiO_2 (110) in the $\bar{\Gamma}\bar{Y}$ azimuth at $T_s=500$ K. The upper panel presents the data in an extended SBZ plot; the lower panel shows the same data in a reduced SBZ plot. The reciprocal lattice points $G_{1,0}=0.966 \text{ \AA}^{-1}$ and $G_{\bar{1},0}=-0.966 \text{ \AA}^{-1}$ and the boundaries of the first SBZ are at $\pm 0.48 \text{ \AA}^{-1}$. Note that the data extend to 100% of the SBZ boundary.

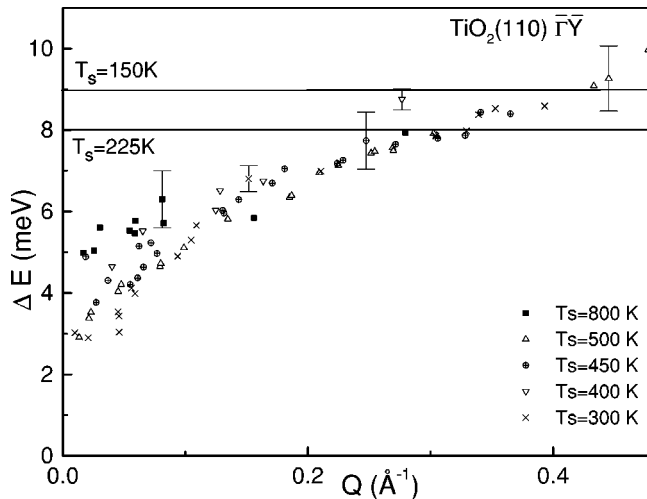


FIG. 24. Reduced SBZ phonon dispersion curves for rutile TiO_2 (110) in the $\bar{\Gamma}Y$ azimuth for all target temperatures measured. The temperatures associated with each symbol are identified in the legend in the figure. Note that the data extend to nearly 100% of the first SBZ. The 150 K and 225 K data are represented only by their fitted lines from Fig. 22. Representative errors are given for each of the substrate temperatures.

presented in Fig. 22 and, for comparison, the dispersion curve at $T_s = 500$ K shown in Fig. 23. Figure 24 contains the dispersion curves for the entire series in this direction at 150, 225, 300, 400, 500, and 800 K. In comparison with the experiments in the other azimuths, the TOF single-phonon peak intensities at all surface temperatures tended to be weak.

Unlike the measurements in the other azimuths, the data for $\bar{\Gamma}Y$ spanned the entire SBZ from zone center to zone boundary. As the results in Figs. 22 and 24 indicate, the vibrational mode appears to be dispersive for surface temperatures 300 K and above, but nondispersive or Einstein like for surface temperatures below 300 K.

The extrapolated energies at the zone center are plotted in Fig. 15(c) as a function of surface temperature. The scatter in the data is real and caused by the weak signals in this direction. Nonetheless, as in the $\bar{\Gamma}S$ direction, the zone-center energy of the mode appears first to soften and then to harden with increasing sample temperature.

Figure 25 shows a semilog plot, for one series of measurements, of the relative intensities of the TOF single-phonon peaks as a function of the parallel momentum transfer. The falloff in intensity is, again, characteristic of a surface mode with polarization perpendicular to the surface.⁵⁸ The corresponding MgF_2 calculations in this azimuth show two low-energy sagittal plane surface modes as in the case for the $\bar{\Gamma}S$ azimuth. The surface-normal vibration is dispersive, whereas the surface parallel vibration has only slight dispersion.³⁰ The measurements suggest that HAS is probing the perpendicular vibrational mode although in this case Pelg *et al.* do not indicate which ions are involved in the motion. The weak intensities of the low-surface-temperature TOF peaks do not permit a meaningful plot to determine whether their polarization is the same as for the dispersive, higher-temperature vibrational modes.

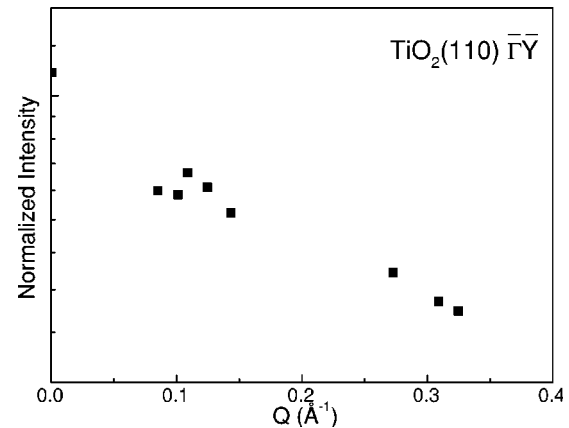


FIG. 25. Semilog plot of the relative surface phonon peak intensity vs momentum transfer from the TOF data taken in the $\bar{\Gamma}Y$ direction for a substrate temperature of 450 K. The characteristic drop off in intensity is indicative of a vibrational displacement polarized normal to the surface (Ref. 58). Note that only a representative sample of the data points have been included in this plot.

V. CONCLUSIONS

A. Structure

The structural features of the TiO_2 (110) surface were primarily determined by AD measurements. The following is a summary of the principal conclusions of this work

(i) The AD measurements taken in the three symmetry directions of the SBZ, $\bar{\Gamma}X$, $\bar{\Gamma}S$, and $\bar{\Gamma}Y$, yield helium atom diffraction peaks corresponding to the lattice spacings predicted from the terminated bulk structure to within the resolution of the instrument ($\sim 1\%$). This is basically in agreement with the results of Diebold and co-workers^{31,47} for the UHV-annealed surface preparation protocol.

(ii) The locations of diffraction peaks in reciprocal space remain unchanged to within the resolution of the instrument over the surface temperature range of ~ 100 – 1000 K.

(iii) The previously reported (4×1) reconstruction in scanning tunneling microscopy experiments⁴⁷ has been observed in AD's on two samples under fortuitous conditions. The very small fourth-order diffraction peaks indicate that this reconstructed region constitutes a minor fraction of the surface.

(iv) The intensity of the specular beam is found to follow the Debye-Waller relation. However, because of the uncertainty in the theory for identifying the mass of the helium atom scatterer for the complex rutile surface, the Debye temperature cannot be definitively obtained. We have arbitrarily assigned mass 80, the mass of a TiO_2 unit, to the scatterer and thereby calculated the Debye temperature to be $\theta_D = 310$ K.

B. Dynamics

We have presented the first HAS study on the dynamics of the TiO_2 (110) surface over much of the SBZ, in the $\bar{\Gamma}X$, $\bar{\Gamma}S$, and $\bar{\Gamma}Y$ azimuths and as a function of surface temperature. Our results are interpreted in part by comparisons with

a theoretical study of rutile $\text{MgF}_2(110)$ (Ref. 30) and with experimental bulk lattice dynamics.²⁶

The following is a summary of the principal findings.

(i) TOF experiments have been carried out in the three high-symmetry azimuths of the SBZ for surface temperatures in the range 150–1000 K, which have led to the determination of surface phonon dispersion curves in these regions.

(ii) In the $\overline{\Gamma X}$ and $\overline{\Gamma S}$ azimuths, the vibrational modes are dispersive over the entire temperature range. In the $\overline{\Gamma Y}$ azimuth the modes found in the experiments at 300 K and higher are dispersive, whereas the modes found below 300 K are dispersionless.

(iii) In all three azimuths the single-phonon TOF intensity vs momentum transfer plots are characteristic of surface phonon modes predominantly polarized perpendicular to the surface; that is, the intensities decrease sharply with increasing phonon wave vector. The very rapid drop-off in intensities suggests, further, that these modes may be hybridizing to some extent with bulk modes of the same symmetry as ΔK increases from the zone center.

(iv) In the $\overline{\Gamma X}$ and $\overline{\Gamma S}$ directions, the data obtained in the TOF spectra span only about 35%–40% of the SBZ from the zone center. In the $\overline{\Gamma Y}$ direction, on the other hand, the data span the entire SBZ. This is consistent with hybridization in the $\overline{\Gamma X}$ and $\overline{\Gamma S}$ azimuths noted in (iii). However, model calculations for this surface are probably required for a definitive explanation.

(v) The extrapolated zone-center phonon energies in the $\overline{\Gamma X}$ azimuth show a distinct softening trend as the temperature of the surface is increased. However, in the other two azimuths, the energies at the zone center appear to soften initially and then stiffen as the temperature is increased. While similar features have been observed in bulk sample studies, their relation to crystalline surface dynamics is not clear.^{62,63} In the experiments here the minimum zone-center phonon energy occurs at ~ 300 K, which is about the same temperature that the dispersionless modes in $\overline{\Gamma Y}$ become dispersive. These results, taken together with other elastic scattering experiments to determine the step heights of adjacent terraces,⁴⁶ suggest that something is happening at the rutile surface in the temperature regime near 300 K.

The zone-center softening and hardening behavior seems to be localized to the (110) surface of rutile TiO_2 , since effects analogous to these have not been observed for the bulk crystal. We can rule out reconstruction since the Bragg diffraction does not reveal changes in the surface reciprocal lattice. Additional experimental evidence is clearly required.

It is our hope and expectation that the results reported here will encourage model calculations for this complex and interesting surface.

ACKNOWLEDGMENT

We gratefully acknowledge the support of this research by U.S. DOE Grant No. DE-FG02-97ER45635.

-
- ¹U. Garibaldi, A.C. Levi, R. Spadacini, and G.E. Tommei, *Surf. Sci.* **48**, 649 (1975).
- ²F.O. Goodman and H. Wachman, *Dynamics of Gas Surface Scattering* (Academic, New York, 1976).
- ³H. Hoinkes, *Rev. Mod. Phys.* **52**, 933 (1980) and referenced cited therein.
- ⁴G. Boato and P. Cantini, *Adv. Electron. Electron Phys.* **60**, 95 (1983) and references cited therein.
- ⁵T.S. Chen, F.W. de Wette, and G.P. Alldredge, *Phys. Rev. B* **15**, 1167 (1977).
- ⁶G. Benedek, G.P. Brivio, L. Miglio, and V.R. Velasco, *Phys. Rev. B* **26**, 497 (1982).
- ⁷J.P. Toennies, in *Surface Phonons*, edited by W. Kress and F. W. de Wette (Springer-Verlag, Heidelberg, 1991), Chap. 5.
- ⁸J.R. Manson, in *Helium Atom Scattering from Surfaces*, edited by E. Hulpke (Springer, Berlin, 1992), p. 173.
- ⁹R.B. Doak, Ph.D. thesis, MIT, 1981.
- ¹⁰R.B. Doak, in *Single Phonon Inelastic Scattering, in Atomic and Molecular Beam Methods*, edited by G. Scoles (Oxford University Press, New York, 1992), Vol. 2.
- ¹¹G. Brusdeylins, R.B. Doak, and J.P. Toennies, *Phys. Rev. B* **27**, 3662 (1983).
- ¹²J.L. Longueville, P.A. Thiry, J.J. Pireaux, and R. Caudano, in *PHONONS 89*, edited by S. Hunklinger, W. Ludwig, and G. Weiss (World Scientific, Singapore, 1990), p. 895.
- ¹³G. Benedek, G. Brusdeylins, V. Senz, J.G. Skofronick, J.P. Toennies, F. Traeger, and R. Vollmer, *Phys. Rev. B* **64**, 125421 (2001).
- ¹⁴D.R. Jung, J. Cui, and D.R. Frankl, *J. Vac. Sci. Technol. A* **9**, 1589 (1991).
- ¹⁵J.P. Toennies, G. Witte, A.M. Shikin, and K.H. Rieder, *J. Electron Spectrosc. Relat. Phenom.* **64/65**, 677 (1993).
- ¹⁶W.P. Brug, G. Chern, J. Duan, G.G. Bishop, S.A. Safron, and J.G. Skofronick, *J. Vac. Sci. Technol. A* **10**, 2222 (1992).
- ¹⁷C. Oshima, *Mod. Phys. Lett. B* **5**, 381 (1991).
- ¹⁸G. Witte, P. Senet, and J.P. Toennies, *Phys. Rev. B* **58**, 13 264 (1998).
- ¹⁹F.W. de Wette, in *Surface Phonons*, edited by W. Kress and F.W. de Wette (Springer-Verlag, Heidelberg, 1991), Chap. 4.
- ²⁰J. Fritsch and U. Schröder, *Phys. Status Solidi B* **215**, 827 (1999).
- ²¹J.A. Li, E.A. Akhadow, J. Baker, L.A. Boatner, D. Bonart, F.A. Flaherty, J. Fritsch, S.A. Safron, U. Schroeder, J.G. Skofronick, T.W. Trelenberg, and D.H. Van Winkle, *Phys. Rev. Lett.* **86**, 4867 (2001).
- ²²R. Reiger, Ph.D. thesis, University of Regensburg, 1986.
- ²³J. Prade, U. Schröder, W. Kress, F.W. de Wette, and A.D. Kulkarni, *J. Phys.: Condens. Matter* **5**, 1 (1993).
- ²⁴J.P. Toennies and R. Vollmer, *Phys. Rev. B* **44**, 9833 (1991).
- ²⁵Jaime A. Li, E.A. Akhadow, Jeff Baker, L.A. Boatner, D. Bonart, J. Fritsch, S.A. Safron, U. Schröder, J.G. Skofronick, and T.W. Trelenberg, *Phys. Rev. B* (to be published).
- ²⁶J.G. Traylor, H.G. Smith, R.M. Nicklow, and M.K. Wilkinson, *Phys. Rev. B* **3**, 3457 (1971).
- ²⁷F. Gervais and W. Kress, *Phys. Rev. B* **28**, 2962 (1983).
- ²⁸Ch. Lee, P. Ghosez, and X. Gonze, *Phys. Rev. B* **50**, 13 379 (1994).

- ²⁹F. Gervais and W. Kress, Phys. Rev. B **31**, 4809 (1985).
- ³⁰G. Pelg, U. Schroeder, W. Kress, and F.W. de Wette, J. Electron Spectrosc. Relat. Phenom. **64/65**, 769 (1993).
- ³¹M. Li, W. Hebenstreit, and U. Diebold, Phys. Rev. B **61**, 4926 (2001).
- ³²E.L.D. Hebenstreit, W. Hebenstreit, and U. Diebold, Surf. Sci. **461**, 87 (2000).
- ³³Jeff Baker, Jaime A. Li, J.G. Skofronick, and S.A. Safron, Phys. Rev. B **60**, 2011 (1999).
- ³⁴A.P. Graham, M.F. Bertino, F. Hofmann, W. Silvestri, and J.P. Toennies, J. Chem. Phys. **106**, 2502 (1996).
- ³⁵D. Fuhrmann, A.P. Graham, L. Criswell, H. Mo, B. Matthies, K.W. Herwig, and H. Taub, Surf. Sci. **482-485**, 77 (2001).
- ³⁶R. Gerlach, G. Polanski, and H.-G. Rubahn, Thin Solid Films **318**, 270 (1998).
- ³⁷Sanford A. Safron, *Advances in Chemical Physics XCV* (Wiley, New York, 1996), pp. 129–212.
- ³⁸Rudolf David Klaus Kern, Peter Zeppenfeld, and George Comsa, Rev. Sci. Instrum. **57**, 2771 (1986).
- ³⁹G. Chern, J.G. Skofronick, W.P. Brug, and S.A. Safron, Phys. Rev. B **39**, 12 828 (1989).
- ⁴⁰L. Pedemonte and G. Bracco, Surf. Sci. **513**, 308 (2002).
- ⁴¹Galileo Electro-Optics Corp., Sturbridge, MA 01566, USA.
- ⁴²National Instruments, Austin, TX 78730, USA.
- ⁴³V.E. Henrich and P.A. Cox, *The Surface Science of Metal Oxides* (Cambridge University Press, Cambridge, England, 1994).
- ⁴⁴R.W. Wyckoff, *Crystal Structures* (Interscience, New York, 1960), p. 7.
- ⁴⁵Commercial Crystal Laboratories, Inc., <http://www.crystalguru.com>
- ⁴⁶Elshan A. Akhadov, Ph.D. thesis, Florida State University, 2002.
- ⁴⁷U. Diebold, J. Lehman, T. Mahmoud, M. Kuhn, G. Leonardelli, W. Hebenstreit, M. Schmid, and P. Varga, Surf. Sci. **411**, 137 (1998).
- ⁴⁸H.-Yang, G.-C. Wang, and T.-M. Lu, *Diffraction from Rough Surfaces and Dynamic Growth Fronts* (World Scientific, Singapore, 1993), p. 23.
- ⁴⁹A.W. Czanderna, C.J. Powell, and T.E. Madey, *Specimen Handling, Preparation, and Treatments in Surface Characterization* (Kluwer Academic–Plenum, New York, 1998).
- ⁵⁰R.A. Bennett, S. Poulston, P. Stone, and M. Bowker, Phys. Rev. B **59**, 10 341 (1999).
- ⁵¹M. Ezell, Undergrad Honors Chemistry Project (private communication).
- ⁵²*Atomic and Molecular Beam Methods*, edited by Giacinto Scoles (Oxford University Press, New York, 1992), Vol. II.
- ⁵³J.R. Manson, Phys. Rev. B **43**, 6924 (1991).
- ⁵⁴G.G. Bishop, E.S. Gillman, Jeff Baker, J.J. Hernández, S.A. Safron, J.G. Skofronick, Srilal M. Weera, and J.R. Manson, Phys. Rev. B **52**, 13 229 (1995).
- ⁵⁵W. Allison, R.F. Willis, and M. Cardillo, Phys. Rev. B **23**, 6824 (1981).
- ⁵⁶E.A. Akhadov, T.W. Trelenberg, S.A. Safron, J.G. Skofronick, D.H. Van Winkle, F.A. Flaherty, and W. Theis, Phys. Rev. B **67**, 113406 (2003).
- ⁵⁷Srilal M. Weera, J.R. Manson, Jeff Baker, E.S. Gillman, J.J. Hernández, G.G. Bishop, S.A. Safron, and J.G. Skofronick, Phys. Rev. B **52**, 14 185 (1995).
- ⁵⁸V. Celli, G. Benedek, U. Harten, and J.P. Toennies, Surf. Sci. **143**, L376 (1984).
- ⁵⁹Notation of bulk TiO₂ directions differ from those of the surface MgF₂(110) used in this work.
- ⁶⁰W. Cochran, *The Dynamics of Atoms in Crystals* (Edward Arnold, London, 1973).
- ⁶¹D. Eichenauer, U. Harten, J.P. Toennies, and V. Celli, J. Chem. Phys. **86**, 3693 (1987).
- ⁶²G. Burns and B.A. Scott, Phys. Rev. Lett. **25**, 167 (1970).
- ⁶³J.A. Gonzalo, Phys. Rev. **144**, 662 (1966).